Neurophotonics

Neurophotonics.SPIEDigitalLibrary.org

Thermal impact of near-infrared laser in advanced noninvasive optical brain imaging

Mina Nourhashemi
Mahdi Mahmoudzadeh
Fabrice Wallois

SPIE.

Neurophotonics 3(1), 015001 (Jan–Mar 2016)

Thermal impact of near-infrared laser in advanced noninvasive optical brain imaging

Mina Nourhashemi, Mahdi Mahmoudzadeh, and Fabrice Wallois*
Université de Picardie, INSERM U 1105, GRAMFC, CHU Sud, rue René Laennec, 80054 Amiens Cedex 1, France

Abstract. The propagation of laser light in human tissues is an important issue in functional optical imaging. We modeled the thermal effect of different laser powers with various spot sizes and different head tissue characteristics on neonatal and adult quasirealistic head models. The photothermal effect of near-infrared laser (800 nm) was investigated by numerical simulation using finite-element analysis. Our results demonstrate that the maximum temperature increase on the brain for laser irradiance between 0.127 (1 mW) and 12.73 W/cm^2 (100 mW) at a 1 mm spot size, ranged from 0.0025°C to 0.26°C and from 0.03°C to 2.85°C at depths of 15.9 and 4.9 mm in the adult and neonatal brain, respectively. Due to the shorter distance of the head layers from the neonatal head surface, the maximum temperature increase was higher in the neonatal brain than in the adult brain. Our results also show that, at constant power, spot size changes had a lesser heating effect on deeper tissues. While the constraints for safe laser irradiation to the brain are dictated by skin safety, these results can be useful to optimize laser parameters for a variety of laser applications in the brain. Moreover, combining simulation and adequate *in vitro* experiments could help to develop more effective optical imaging to avoid possible tissue damage. [DOI: 10.1117/1.NPh.3.1.015001]

Keywords: near-infrared laser; optical imaging; photothermal effect; neonatal head model.

Paper 15027RR received May 22, 2015; accepted for publication Dec. 3, 2015; published online Jan. 14, 2016.

1 Introduction

Conventional optical imaging systems typically include certain basic components such as various types of lasers and flexible fiber optics.[1] Over recent decades, optical methods have been used to monitor brain function,[2] neurovascular coupling that is correlated to brain activity, brain hemodynamics, cerebral blood volume, and oxygenation.[3,4] Such modalities have a broad range of practical imaging applications in both adults and neonates,[5,6] particularly in premature neonates,[7,8] ranging from changes in tissue oxygenation (by near-Infrared spectroscopy) and cerebral blood flow (CBF) measurement [by diffuse correlation spectroscopy (DCS)][9,10] to changes in membrane configuration such as neuron swelling and shrinking (fast optical signal).[11] The photothermal impact of lasers is a critical parameter that needs to be determined in order to evaluate the effectiveness and laser safety of these systems especially with high power consumption (50,[12–15] ~60,[16] and 300 mW).[17] Laser has photothermal interactions with tissues[18] caused by the temperature rise due to laser irradiation, which may cause damage to the tissues,[19] including protein denaturation, increased mitochondrial membrane permeability, and ultimately vaporization.[20] Temperature increase can also lead to changes in cellular metabolism, electrical membrane capacitance, and in the long term, can lead to necrosis.[21–26] However, the mechanisms responsible for tissue damage from heat exposure are complex and still poorly understood. Although no obvious thermal impacts are detected at skin temperatures of 37°C to 41°C, a temperature increase above 41°C and up to 50°C likely results in reversible membrane alterations.[25,27,28] The normal skin surface temperature, depending on environmental conditions, is usually around 31°C; a sustained temperature increase by >10°C can, thus lead to tissue damage.[26,29] Irreversible mechanisms then occur, resulting in cell death.[28] The temperature known to induce cell injury is 10°C when studied *in vitro*, resulting in vascular damage such as angiogenesis or necrosis (3°C),[22] aberrant neuronal activity in guinea pig olfactory cortical slices (2°C),[21] cortical spreading depression (3.4°C),[30] or axonal injury (1°C). Furthermore, temperature increases >1°C can have long-term effects on brain tissue.[24,31]

The propagation of laser light energy through the tissues is, therefore, an important issue in optical imaging. Effective functional optical imaging can be achieved by tailoring the laser parameters to the optical characteristics of the target tissue (heat capacity, thermal conductivity, absorption coefficient, and scattering coefficient). Laser parameters (e.g., radiant energy, frequency, spot size, and pulse duration) should be carefully chosen to optimize imaging efficacy while minimizing undesirable tissue damage. The energy delivered to the tissues must be determined in order to ensure safety standards in optical imaging. The specific limits of laser power that determine the harmful effects of heat on neonatal tissue are poorly elucidated. Due to the specificity of neonatal head tissues, such as thin skin and skull, tissue absorption coefficients may be different from those observed in adults.[32] It is, therefore, essential to test the safety of optical imaging lasers in this specific, sensitive population.

The purpose of this study was to model the photothermal interaction of NIR laser on human tissues. We investigated the influence of heat and fluence rate of various laser radiant powers on two head models (adult versus neonate). The temperature distribution inside the tissue was modeled using finite element method simulations and the bioheat transfer equation to determine the transient temperature function required to

---

*Address all correspondence to: Fabrice Wallois, E-mail: Fabrice.wallois@u-picardie.fr

Table 1 MPE for skin exposure to a laser beam (from ANSI Z136.1-2014).

Wavelength (nm)	Exposure time, t (s)	MPE
400 to 1400	10^{-7} to 10	$1.1 \times \mathrm{CA} \times t^{0.25}$ (J/cm^{-2})
400 to 1400	10 to 3.0×10^4	$0.2 \times \mathrm{CA}$ (W/cm^{-2})

Note: t is the laser exposure duration, $\mathrm{CA} = 10^{0.002(\lambda - 700)}$.

calculate the photothermal interaction. A range of different laser powers (1 to 100 mW) with various spot sizes, different skin and brain absorption coefficients, temperature distribution profiles in adults versus neonates, and the influence of blood perfusion were investigated using the simulated model. Laser irradiation was simulated using the diffusion theory and was validated by comparing with Monte Carlo method.

Laser wavelength and power are the effective parameters in tissue-delivered energy. These properties, using wavelengths longer than 950 nm, have been extensively used for laser surgery.[33] In this paper, we investigate the effect of lasers on neonatal and adult head tissues in the lower NIR spectrum (600 to 900 nm) used in functional optical imaging. We also discuss our mathematical approach and its limitations.

The laser hazard class depends on the potential to cause biological damage (ANSI Z136.1-2014, IEC 825-1).[34] Accessible emission limit (AEL) and maximum permissible exposure (MPE) for a given wavelength and exposure time were considered to evaluate the risk of injury (Table 1) (AEL = MPE × Area of Limiting Aperture). According to the above standards, the MPE (frequency and time dependent) is the highest power (W/cm^2) of a light source that is considered to be safe and is usually about 10% of the dose associated with a 50% chance of causing damage[35] under worst-case conditions.

According to ANSI,[36] the 3.5-mm limit aperture diameter of irradiated laser was selected as for NIR exposures to the skin lasting longer than 10 s, involuntary movements of the body and heat conduction will result in an average irradiance profile over an area of about 10 mm^2 (even when the irradiated body part is intentionally kept still).[37]

2 Materials and Methods

To evaluate the thermal impact of NIR laser light in optical imaging in human head tissues, we used finite-element analysis (FEA), using the laser radiant power and exposure time. Two quasirealistic six-layered models of neonatal and adult head tissues were simulated during irradiation by a focal infrared laser beam. To simulate the thermal interaction due to laser irradiation by different laser radiant powers and head model tissues (neonate versus adult), the bioheat diffusion model was calculated by finite-element solver COMSOL multiphysics. The resulting thermal distribution under steady-state conditions and their time profiles were investigated. As blood flow is a factor with a major impact on heat, we further investigated the influence of blood perfusion on local heating induced by laser irradiation.

2.1 *Numerical Analysis and Modeling of Heat Transfer in the Tissues due to the Laser Source*

Heat transfer from the laser source to the surrounding tissues was simulated by using the FEA method and bioheat equation. This model includes heat conduction, convection through blood flow, metabolic heat generation in the tissue, and heat generation by the laser source. In this model, the tissues were assumed to be homogeneous and isotropic. The temperature distribution was obtained by solving the bioheat transfer equation[38]

$$C\rho \frac{\partial T}{\partial t} = \nabla.(k\nabla T) + A_0 - B_0(T - T_B) + Q_{\mathrm{ext}}\left(\frac{w}{m^3}\right), \tag{1}$$

where T is the temperature (°C), C is the specific heat [J/(kg/°C)], ρ is the tissue density (kg/m^3), k is the thermal conductivity [J/(m s/°C)], A_0 is the basic metabolic rate [J/(m^3/s)], B_0 ($\rho_b c_b \omega_b$) is the blood perfusion coefficient [J/(m^3/s/°C)] that includes blood specific heat C_b(j/kg K), blood perfusion rate w_b(1/s), and mass density of blood ρ_b(k/m^3), T_B is the temperature of blood (°C), and Q_{ext} is the external heat source (W/m^3). This equation computed the temperature distribution within the tissue at different times during laser irradiation.

To solve the bioheat equation, the boundaries of the model, except for the surface of the skin layer exposed to air, were considered to be at body temperature. At the surface in contact with air, it was assumed that heat transfer occurred as a result of free convection into air (heat transfer by radiation into the air would be negligible), which is described by

$$n.(k\nabla T) = h(T_{\mathrm{ext}} - T), \tag{2}$$

where n is the outward normal vector, h is a heat transfer coefficient to control convective cooling to the model (W/m^2/K), defined as 5 W/m^2/K for air, T_{ext} is the external temperature defined as 24°C for air, T is the internal temperature of model, and k is the thermal conductivity (W/m/K).[39,40]

2.2 *Modeling the Laser Source*

To simulate the heat generated by the laser irradiation (the source term Q_{ext}), a spatially Gaussian and temporally continuous laser beam was modeled perpendicular to the surface of the model to simulate an optical fiber positioned orthogonally to the surface.

Light propagation in biological tissue results from the diffusion approximation of the radiative transfer equation and is defined by[41]

$$\frac{1}{c}\frac{\mathrm{d}}{\mathrm{d}t}\phi(r,t) - \nabla\left[\frac{1}{3(\mu_a + \mu_s)}\right]\nabla\phi(r,t) + \mu_a\phi(r,t) = S(r,t), \tag{3}$$

where c is the light speed in a vacuum, μ_a is the absorption coefficient, μ_s is the reduced scattering coefficient, ϕ is the photon intensity, and $S(r,t)$ is the local photon source ($Q_{\mathrm{ext}} = \mu_a\phi$). The photon-diffusion equation was used to calculate photon propagation in strong-scattering media such as biological tissues. The diffusion approximation can correctly predict light transport in a region far from the laser source, where all photons are scattered at least several times.[42,43] In skin, these conditions are only satisfied in the deeper levels of the dermis and do not apply to the epidermis, where scattering of radiation remains highly anisotropic. A skin depth of 0.4 mm was, therefore, used for further skin investigation. Different power levels were investigated and the results were compared between neonatal and

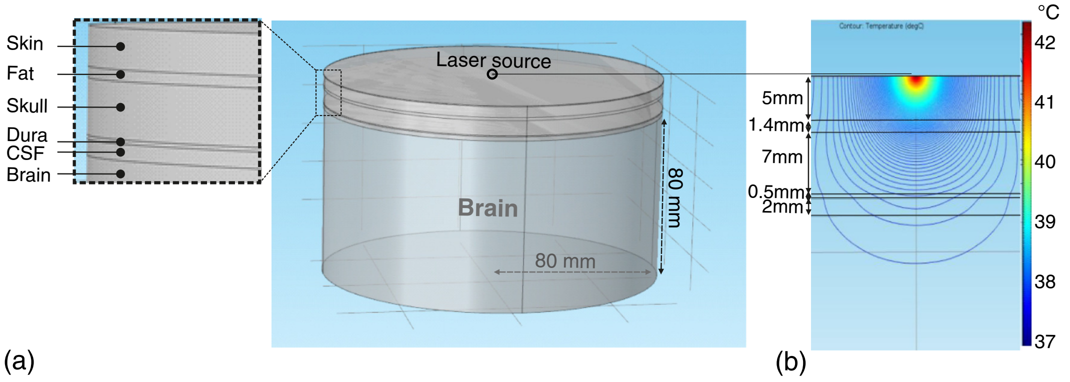

Fig. 1 (a) Geometrical structure of 3-D-CAD composed of six layers (skin, fat, skull, dura, CSF, and brain) (inset shows a zoom up region). The origin was situated immediately under the source. (b) Distributions of the photon-fluence rate in the head calculated in the head model.

adult head models. Dirichlet and Robin boundary conditions were applied by

$$\phi(r,t) = 0, \tag{4}$$

$$\phi(r,t) + 2\frac{1}{3(\mu_a + \mu_s)}\frac{1+R}{1+R}\frac{\partial\phi(r,t)}{\partial n} = 0, \tag{5}$$

where n is the normal vector and $(R = 0)$ is the reflection parameter.

2.3 Model

Two quasirealistic six-layer head models in a 3-D Cartesian (x, y, and z) coordinate system were simulated to solve light propagation equations in neonatal and adult head tissues, as shown in Fig. 1. The thickness of the skin, fat, skull, dura, cerebral spinal fluid (CSF), and brain was defined as shown in Table 2 for the adult and neonatal models. The minimum thickness of neonatal skin was extracted from the distribution of skin thicknesses measured *in vitro* as a function of gestational maturity.[50] For the sake of simplicity, the curvature of the six layers was not considered. To assume that the temperature at the boundary of the selected region was equal to body temperature (37°C), a sufficiently large thickness (80 mm) of brain tissue was selected. The model size was defined as (radius = 80 mm and height = 80 mm), fourfold larger than the area affected by laser radiation in order to conserve the semi-infinite nature of the model.[51] The optical source was simulated in which the laser source emits a Gaussian and temporally continuous laser beam. Different radii of laser spots (0.2, 0.4, 0.6, 1, 3, 5, 7, 11, and 15 mm) for different powers (from 10 to 200 mW) were investigated.

The adult and neonatal models consisted of 1,564,530 and 1,024,918 tetrahedral elements, respectively. The maximum element size of the refined mesh around the light source was 0.01 mm. The diffusion equation is valid in the case of large scattering compared with absorption and when studying diffuse light propagation, i.e., at sufficient distances from any light sources. These considerations were applied to the physics of the model.

Table 2 Tissue thickness (mm) of six-layer adult and neonatal head models.

	Skin	Fat	Skull	Dura	CSF	Brain
Adult	5[44–46]	1.4[47,48]	7[44–46]	0.5[48,49]	2[44,47]	80
Neonate	0.5[50]	1.4[47,48]	2[44]	0.5[48,49]	0.5[44]	80

2.4 Thermal and Optical Properties for Various Tissues

The tissue parameters of the model, such as thermal conductivity, density, heat capacity at constant pressure, metabolic rate, blood perfusion for the six different layers, are shown in Tables 3 and 4.[52] The brain perfusion rate used in this study was 0.00932 $\text{s}^{-1} \approx 0.56\ \text{min}^{-1}$, which is comparable with the value measured *in vivo* with ASL-fMRI.[60,61] Gray and white matters were considered to have the same thermal properties.[39] The effect of cerebral metabolism on brain temperature was considered to be negligible,[62,63] allowing the metabolic rate for adults and neonates considered to be identical. Brain function and metabolic activity are indicated by oxygen concentration and glucose intake in brain cells.[64,65]

The NIR laser wavelength in the middle of biological optical windows (600 to 900 nm) was selected for further investigation (isosbestic point: 800 nm).[66] The scattering coefficients were acquired by the following equation:

Table 3 Thermal properties of the six layers of the head (skin, fat, skull, dura, CSF, and brain).[52]

	Thermal conductivity (W/m/K)	Density (kg/m^3)	Heat capacity at constant pressure [J/(kg/K)]
Skin	0.420	1010	3500
Fat	0.250	920	2500
Skull	0.30	1810	1300
Dura[53]	0.44	1174	3364
CSF[2]	0.57	1007	4096
Brain	0.503	1043	3600

Table 4 Heat equation parameters of the six layers of the head (skin, fat, skull, dura, CSF, and brain).[52]

	Blood temperature T_b (K)	Blood specific heat C_b (j/kg K)	Blood perfusion rate w_b (1/s)[52,54–56]	Mass density of blood ρ_b (kg/m^3)	Metabolic rate Q_{met} (W/m^3)
Skin	310.15	3840	0.00257	1060	1000
Fat	310.15	3840	0.00023	1060	180
Skull	310.15	3840	0.00004	1060	0
Dura[2]	310.15	3840	0.00744	1060	6914
CSF[2]	310.15	3840	0	1060	0
Adult brain	310.15	3840	0.00932	1060	10,000
Neonatal brain	310.15	3840	0.00166[57–59]	1060	10,000

$$\mu_s' = a(\lambda/500\ \mathrm{nm})^{-b}, \tag{6}$$

where a, b, and λ are scattering amplitude [related to scatterer density (cm^{-1})], scattering power (related to scatterer size distribution) and wavelength in nm, respectively. a and b coefficients for different tissues were selected according to Ref. 67. Absorption and scattering coefficients of different adult and neonatal tissues are given in Table 5. For the 800 nm wavelength, similar optical properties for neonatal and adult skin were obtained from Refs. 67 and 66, respectively.

Discrepancies were observed concerning the precise value of absorption and scattering coefficients. This difference could be derived from the discrepancy between theoretical and experimental results. In general, *in vivo* μ_a and μ_s values for human skin were significantly smaller than those obtained *in vitro* (about 10 and 2 times, respectively[71]). For μ_a, the discrepancy may be attributed to the low sensitivity of the double-integrating sphere, and goniometric techniques were applied for *in vitro* measurements at weak absorption combined with strong scattering ($\mu_a \ll \mu_s$) and sample preparation methods.

The absorption coefficients in our study were adopted from the most recent complete reference concerning the optical properties of tissues.[66] Different percentages of melanin (Melanosomes per unit volume)% = 0.87%, 1.15%, 1.65% corresponding to the skin absorption coefficient $\mu_{a(\mathrm{skin})} = 0.52$, 0.65, and 0.88 cm^{-1} (Ref. 67) were applied in our model. A wide range of skin absorption coefficients (0.5 cm^{-1} also including 0.1, 0.2, 0.3, and 0.4 cm^{-1}) was investigated. In addition, different ranges (0.01, 0.05, 0.1, and 0.5 cm^{-1}) of adult brain absorption coefficients were considered.[71]

Table 5 Optical properties of the tissue components, corresponding to the six layers of the head (skin, fat, skull, dura, CSF, and brain): absorption coefficient,[66] scattering coefficient.[67–69]

	Absorption coefficients (cm^{-1})	Scattering coefficients (cm^{-1})
Skin	0.52[66,67]	23.58[67]
Fat	0.11[66]	13.41[67]
Skull	0.11[66]	16.35[67]
Dura	0.70[66]	12.61[67]
CSF	0.01[66]	3.2[70]
Adult brain	0.90[66]	11.34[67]
Neonatal skin	0.52[68]	23.58[68]
Neonatal brain	0.08[71]	8.42[71]

3 Results

The first section describes the light-induced heating due to exposure from various laser powers and the distribution profile due to photothermal interactions in various types of adult and neonatal head tissues. The following sections describe the effects of blood perfusion, various skin and brain absorption and scattering coefficients, laser spot size, and different tissue thickness on the temperature distribution in head tissues. Moreover, Monte Carlo simulation was used to validate the diffusion theory.

3.1 *Effect of Various Laser Radiant Powers on Neonatal and Adult Head Models*

Figure 2 shows the various temperature change profiles as a function of the radial distance around an optical fiber tip (laser spot size = 1 mm) in six different layers of the head models (skin, fat, skull, dura, CSF, and brain) under steady-state conditions [Fig. 2(a): adult, Fig. 2(b): neonate]. The maximum temperature increase, using NIR for laser powers between 1 and 100 mW (laser irradiance, I, between 0.127 and 12.73 W/cm^2), with 10 mW increments, ranged from 0.16°C to 16.12°C (on the adult head) and 0.13°C to 13.51°C (on the neonatal head) at a skin depth of 0.4 mm. However, the maximum temperature increase on the brain for laser powers between 1 and 100 mW ranged from 0.0025°C to 0.26°C and from 0.03°C to 2.85°C at depths of 15.9 and 4.9 mm in the adult and neonatal brain, respectively. Figure 2(c) demonstrates the temperature changes at the depth of 0.4 mm with various powers: 10 to 100 mW in 10 mW increments over time.

3.2 *Effect on Neonatal Versus Adult Tissue*

The intensity and correlative temperature changes in adult and neonatal head tissues according to the depth from the surface under steady-state conditions were evaluated in order to compare temperature distribution profiles in the adult versus the

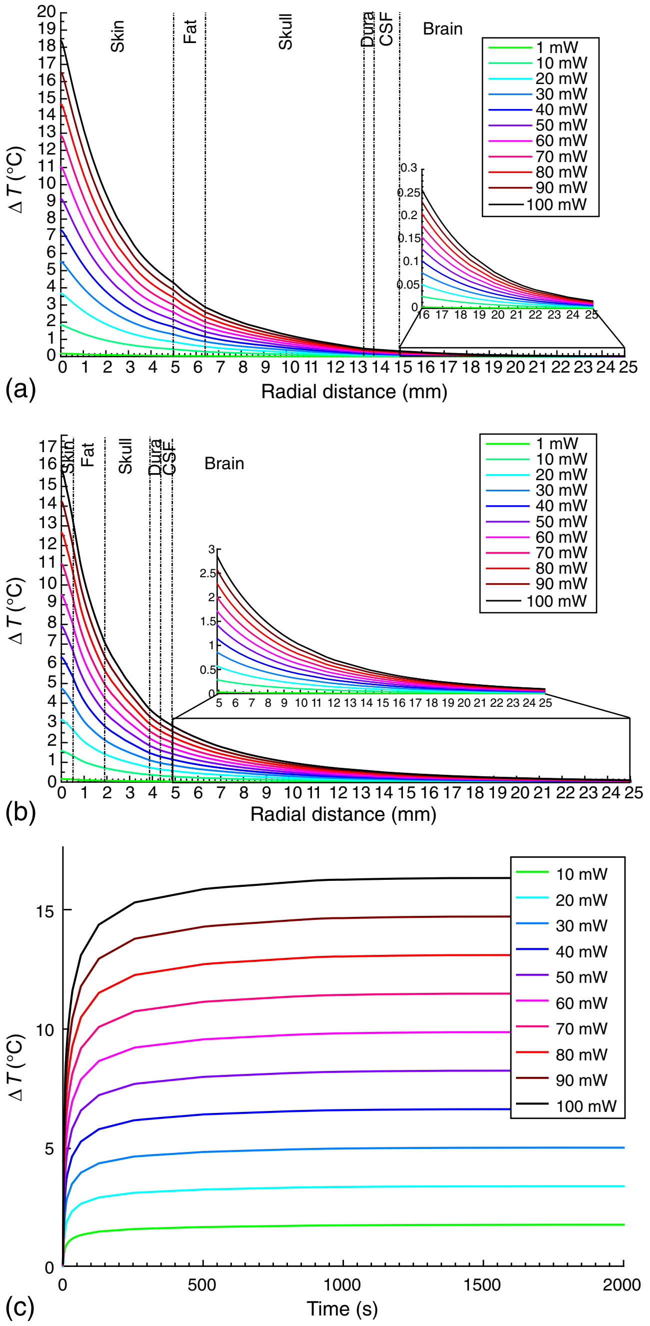

Fig. 2 Temperature changes according to the radial distance from the laser source with various powers: 1 mW, 10 to 100 mW 10 × 10 ($0.127\ \mathrm{W/cm^2} < I < 12.73\ \mathrm{W/cm^2}$), for a six-layered head model (skin, fat, skull, dura, CSF, and brain) obtained from numerical simulations (the inset shows a zoom up region). (a) Adult head model, (b) neonatal head model, and (c) temperature changes at the depth of 0.4 mm with various powers: 10 to 100 mW in 10 mW increments over time.

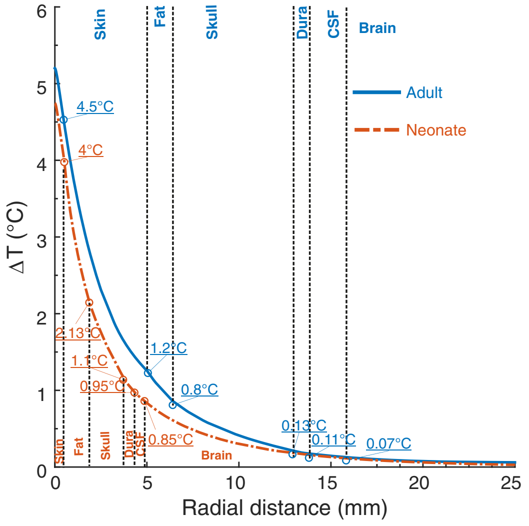

Fig. 3 Temperature changes according to the radial distance from the laser source ($I = 3.81\ \mathrm{W/cm^2}$) for six layers of adult and neonatal head model (skin, fat, skull, dura, CSF, and brain) obtained from numerical simulations.

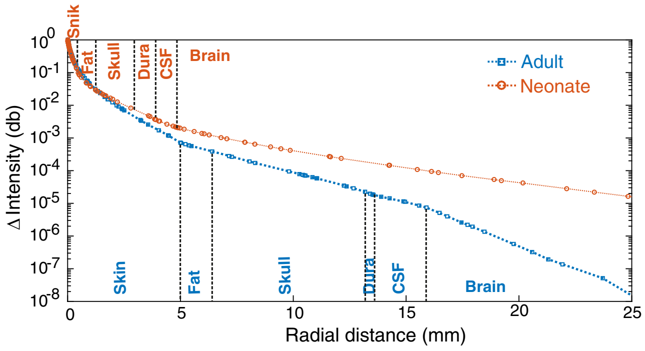

Fig. 4 Comparative distributions of the normalized intensity of photons (I/I_0) according to the radial distance from the laser source ($I = 3.81\ \mathrm{W/cm^2}$) for six layers of adult (lower diagram) and neonatal head models (skin, fat, skull, dura, CSF, and brain) obtained from numerical simulations.

neonatal model (Fig. 3). For instance, Figs. 3 and 4 show the heat distributions for $3.81\ \mathrm{W/cm^2}$ and the magnitude of laser penetration, respectively. As the skin and skull are much thinner in neonates, more light reaches the neonatal brain than the adult brain, which consequently results in a more marked temperature increase in the neonatal than in the adult brain. In the present study, using similar characteristics for neonatal and adult skin, the temperature increase was obviously the same in the two models. Due to the shorter distance of the other tissues from the surface in the neonatal head, the maximum temperature increase for $3.81\ \mathrm{W/cm^2}$ was higher in the neonatal brain ($\Delta T = 0.85$°C) than in the adult brain ($\Delta T = 0.07$°C) (Fig. 3).

The light-distribution profiles on the brain surface for the respective models are presented in Fig. 4, which shows the comparative distributions of the normalized intensity of photons (I/I_0) from the laser source (30 mW) for six layers of adult (lower diagram) and neonatal head models (skin, fat, skull, dura, CSF, and brain). The depths of the brain from the skin surface were 15.9 mm for the adult model and 4.9 mm for the neonatal model. The horizontal axis represents the distance along the surface of the brain from the source. Comparison of the adult and neonatal models showed deeper scattering of light in the neonatal brain.

3.3 *Effect of Blood Perfusion*

As blood flow has a major impact on tissue temperature regulation, we simulated two different conditions (presence and absence of blood perfusion) in the adult model to investigate the influence of blood perfusion on local heating induced by laser irradiation [Fig. 5(a)]. The maximum temperature increase in the brain in the presence of blood perfusion ($\Delta T = 0.07°\mathrm{C}$) was lower than in the absence of blood perfusion ($\Delta T = 0.5°\mathrm{C}$), suggesting that, based on the numerical simulation, blood perfusion decreases the temperature rise by 0.43°C for $3.81\ \mathrm{W/cm^2}$. Figure 5(b) shows the effect of different blood perfusion and metabolic rates on induced heat distribution in neonatal brain. Doubling the blood perfusion rate decreased temperature changes in the brain by about 0.1°C [Fig. 5(b)], whereas the laser-induced heat changes in the brain when the normal adult metabolic rate ($10{,}000\ \mathrm{W/m^3}$) is decreased by one half can be considered to be negligible.

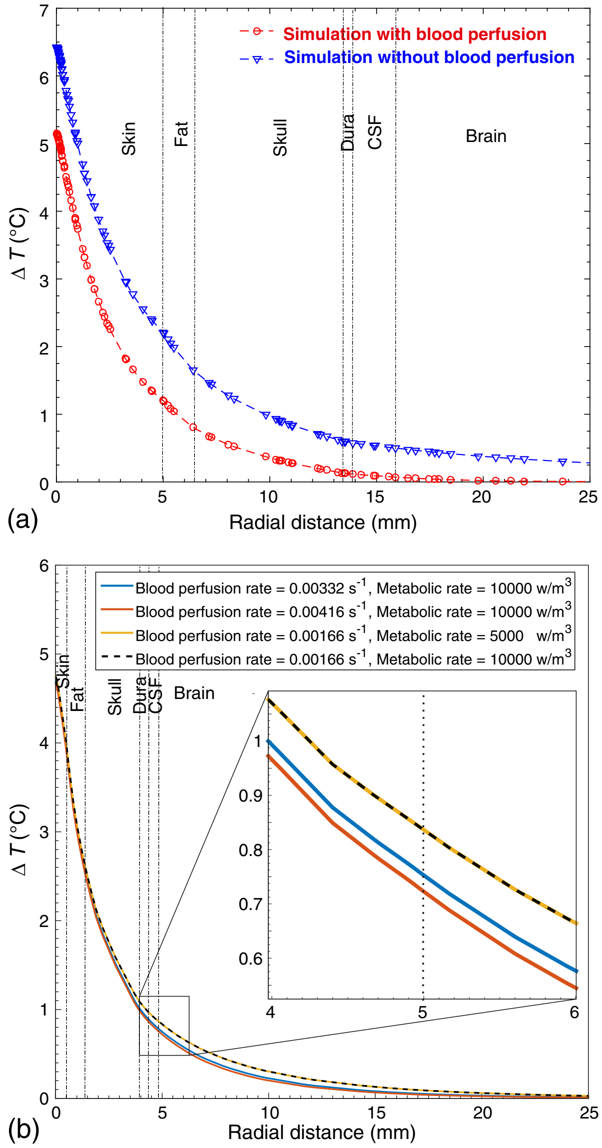

Fig. 5 Comparative temperature changes according to the radial distance from the laser source ($I = 3.81\ \mathrm{W/cm^2}$) between six layers of the head model (skin, fat, skull, dura, CSF, and brain) (a) with blood perfusion and without blood perfusion in adult and (b) the effect of different blood perfusion rates and metabolism on induced heat distribution in neonatal brain.

3.4 *Effect of Different Skin and Brain Absorption Coefficients*

As accurate *in vivo* measurements of optical properties are not available, a wide range of these values had to be modeled. Figure 6 presents the evolution of the temperature profile as function of radial distance for different skin [Fig. 6(a)] and brain [Fig. 6(b)] absorption coefficients for $3.81\ \mathrm{W/cm^2}$. The curves depict the temperature distribution in the skin and brain, in which a variation of the absorption coefficient [$\mu_{a(\mathrm{skin})}$: 0.1 to $0.88\ \mathrm{cm^{-1}}$; $\mu_{a(\mathrm{brain})}$: 0.01 to $0.5\ \mathrm{cm^{-1}}$] had a significant influence at a depth of 0.4 mm in the skin ($\Delta T = 1.8°\mathrm{C}$ to 6.9°C), but not in brain tissue ($\Delta T = 0.07100°\mathrm{C}$ to 0.7148°C).

3.5 *Effect of Different Laser Spot Sizes*

Laser spot size impacts the temperature profile. The effect of laser spot size on the temperature distribution in the skin and brain tissue of the adult and neonatal head models was investigated in the laser power range of 10 to 200 mW (in order to investigate the effect of higher powers on the temperature

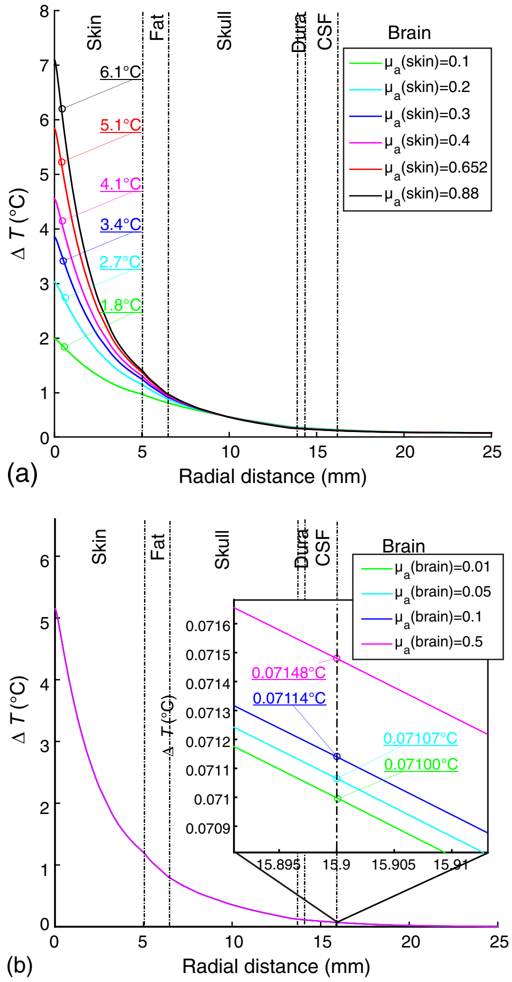

Fig. 6 The temperature changes according to the radial distance from the laser source ($I = 3.81\ \mathrm{W/cm^2}$) with various absorption coefficients are shown; the lines correspond to different (a) skin and (b) brain absorption coefficients. (The inset shows a zoomed up region.)

profile by changing spot size). Figure 7 shows a more marked temperature decrease as the laser spot size was increased from 0.2 to 15 mm.

Figure 8 shows the temperature changes versus irradiance [Fig. 8(a), skin; Fig. 8(b), brain]. Temperature changes in the brain were 0.6059°C and 0.7182°C for the same irradiance of 0.113 $\mathrm{W/cm^2}$ with different powers and spot sizes (150 mW, spot size $= 13$ mm) and (200 mW, spot size $= 15$ mm), respectively. Higher powers and larger spot sizes (but with the same irradiance), therefore, induced higher temperatures, implying that temperature changes depend not only on the magnitude of irradiance but also on the photon distribution (which depends on both power and spot size).

3.6 *Effect of Different Tissue Thicknesses*

Different thicknesses were investigated, as tissue thickness is one of the parameters that needs to be accurate, and they are estimated and variable according to different individuals and medical conditions. Figure 9 shows the analysis of temperature changes in different tissues due to variations of the thickness of individual layers. Temperature changes were not largely affected by variations of the thickness of each layer: skin (3, 4, 5, and 6 mm), fat (0.4, 1.4, 2, and 3 mm), skull (5, 6, 7, and 8 mm), and CSF (0.1, 1, 2, and 3 mm). In particular, the effect of thickness variations on deep tissues is negligible.

3.7 *Validation of Diffusion Theory*

The diffusion theory and the Monte Carlo approach have complementary attributes for modeling photon transport in a scattering medium. The Monte Carlo approach is precise but computationally inefficient, whereas the diffusion theory is inaccurate but computationally efficient. A trade-off must, therefore, be reached between the computational accuracy and efficiency of the two models. Using Monte Carlo improves the computational accuracy at the expense of computational efficiency. Although the diffusion theory is acceptable when the isotropic point source is situated far from the surface of the scattering medium, it becomes less accurate as the source approaches the surface (Fig. 10). To demonstrate this point, we compared the results obtained with the Monte Carlo method[72] and the diffusion theory. In this section, we evaluate each step of the approximation described above using the accurate Monte Carlo method. The optical properties from Table 5 were used. As shown in Fig. 8, the fluence derived from the diffusion theory was only accurate when r was greater than 0.3 cm. Deviations caused by each step of the approximation are illustrated in Fig. 10. Curve M is derived from the Monte Carlo method, whereas curve D is derived from the diffusion theory.

The error due to the approximation of Fig. 10(a) (right) with Fig. 10(b) (left) is shown in Fig. 10(c). Curves M and D were calculated by the Monte Carlo method and the diffusion theory, respectively; they show relatively small systematic differences. The relative error decreased with increasing r; it was >100% close to $r = 0\%$ and 20% close to $r = 0.35$ cm.

4 Discussion

To the best of our knowledge, this is the first study to use two quasirealistic models (six-layered neonatal versus adult head models) to quantify the temperature distribution by bioheat diffusion modeling. Furthermore, despite the use of animal models,[39] this is the first study to use an FEA approach to

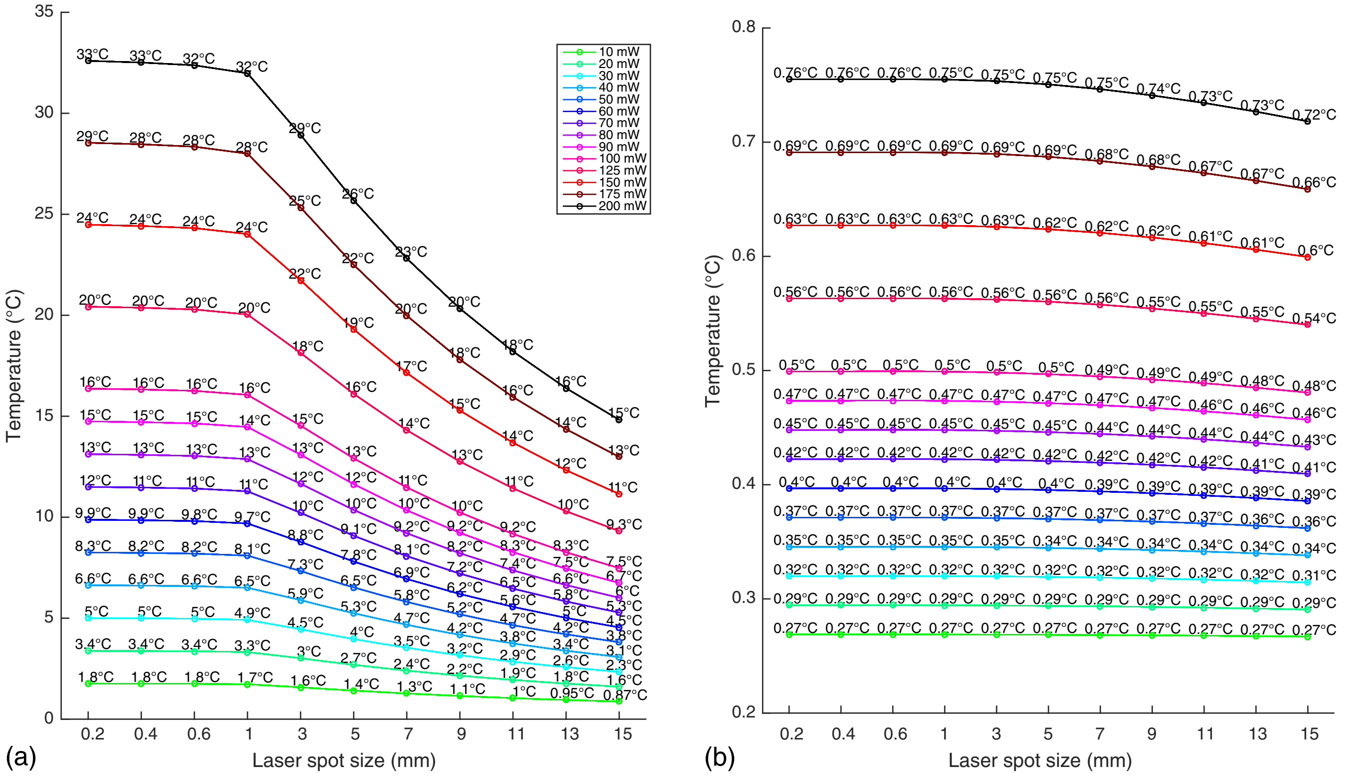

Fig. 7 The effect of laser spot size on the temperature distribution in (a) adult skin and (b) adult brain tissue.

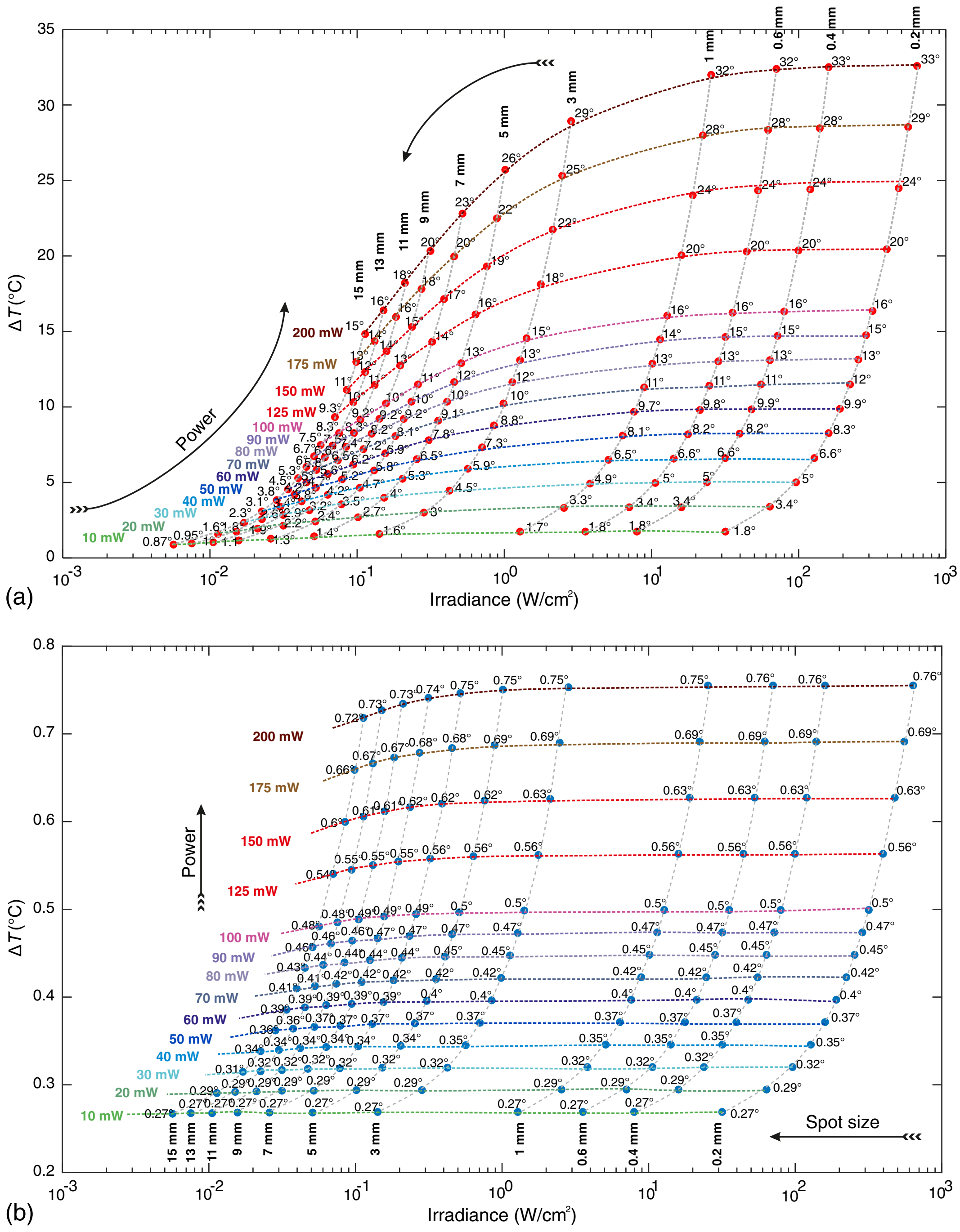

Fig. 8 The effect of laser irradiance on the temperature distribution in (a) adult skin and (b) adult brain tissue.

investigate the influence of heat and fluence rate of various laser radiant powers on human head models (adult and neonatal) with blood perfusion.

4.1 *Effect of Various Laser Radiant Powers on Neonatal and Adult Head Models*

By ignoring the optical discontinuity and anisotropic properties of the tissues, the temperature distribution showed a higher surface temperature for a highly scattering medium during laser irradiation. Current research into laser-induced tissue damage has focused on damage generated in superficial tissues in adults.[26] Ito et al. investigated the heating effect of NIR irradiation at 789 nm. A 0.101°C/mW temperature elevation was detected at a depth of 0.5 mm in the human forearm in which $\mu_{a(\mathrm{forearm})} = 0.2\ \mathrm{cm}^{-1}$.[66]

In agreement with the results of this previous study,[26] our results show a 2.7°C temperature increase at a depth of 0.4 mm in the skin [using $\mu_{a(\mathrm{skin})} = 0.2\ \mathrm{cm}^{-1}$, NIR light at 800 nm, and a power of 30 mW, $I = 3.81\ \mathrm{W/cm}^2$] [Fig. 6(a)]. On the other hand, for a power of 1 mW ($I = 0.127\ \mathrm{W/cm}^2$), a 0.16°C temperature increase was detected at a depth of 0.4 mm in the skin [using $\mu_{a(\mathrm{skin})} = 0.5\ \mathrm{cm}^{-1}$]. In our simulation, the total fluence rate, especially in the superficial area of

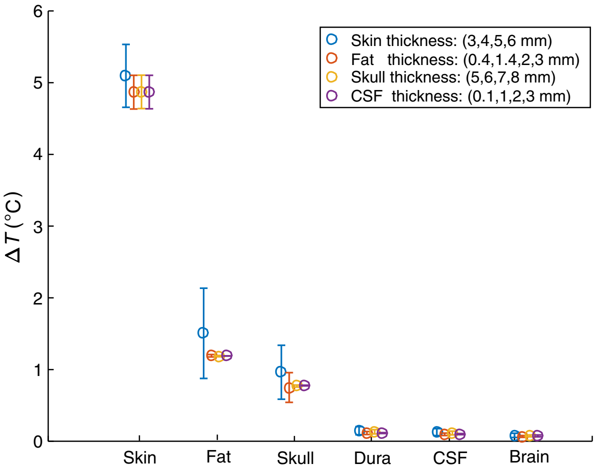

Fig. 9 Temperature changes in different tissues due to variations in the thickness of individual layers.

skin, was overestimated when the diffusion approximation was used.[73] Although the main aim of our study was to investigate thermal effects on brain tissue (situated far away from the laser source), we compared the results obtained in superficial tissue in a previous experimental study in order to validate our model.[26]

In adults, a 10°C temperature increase is considered to be the safety limit to avoid skin injury[74] (assuming a skin surface temperature of around 31°C). Consequently, our results show a temperature increase of up to 10°C at a power of about 50 mW ($I = 6.36\ \mathrm{W/cm^2}$) and 60 mW ($I = 7.63\ \mathrm{W/cm^2}$) under steady-state conditions on adult and neonatal skin, respectively.

Considering a 1-mm spot size and assuming a brain blood perfusion rate equal to $0.00166\ \mathrm{s^{-1}}$, the temperature increase in the adult brain for powers ranging from 1 to 100 mW ($0.127\ \mathrm{W/cm^2} < I < 12.73\ \mathrm{W/cm^2}$) was much lower ($\Delta T = 0.002°\mathrm{C}$ to $0.26°\mathrm{C}$) than the temperature known to induce cell injury when studied *in vitro* (10°C). In contrast, in the neonatal brain, the temperature increase was lower ($\Delta T = 0.03°\mathrm{C}$ to 0.86°C) than the critical temperature (1°C) for powers ranging from 1 to 30 mW ($0.127\ \mathrm{W/cm^2} < I < 3.81\ \mathrm{W/cm^2}$) and a 1-mm spot size.

4.2 Effect on Neonatal Versus Adult Tissue

As expected, with an irradiance of $0.31\ \mathrm{W/cm^{-2}}$, the temperature increase in the neonatal brain was higher than that in the adult brain (when comparing the ΔT of each neonatal head layer with the same layer in the adult model), notably because of the thinner skin and skull in neonates, facilitating penetration of photons into the brain. Despite similar optical properties of neonatal and adult skin at 800 nm,[50,66] additional factors predisposing to a more marked temperature increase are the greater transparency and lower absorption coefficient of neonatal brain tissues.[71]

Nevertheless, the temperature increase at $3.81\ \mathrm{W/cm^2}$ was about 4.5°C versus 4°C at a depth of 0.4 mm in skin (neonate versus adult) and 0.85°C versus 0.07°C on the brain (neonate versus adult), which is still much lower than the previously reported limit for the skin (10°C) and the brain (1°C) under steady-state conditions[24] and also well below the safety limits adopted for laser-induced tissue injury. However, if the temperature changes very slowly (e.g., at a rate of less than 0.5°C/ min), the subject may be unaware of a 4°C to 5°C change in temperature[75] provided the skin temperature remains within the neutral thermal range of 30°C to 36°C.

4.3 Effect of Blood Perfusion

Blood perfusion plays a significant role in the thermal regulation of a living body. In this study, blood perfusion removed heat away from the laser source and appeared to constitute a cooling mechanism for the brain. Local heating of the model was considerably reduced when blood perfusion in the tissues was taken into account. Body fluids, transporting heat throughout the tissues, act as a convection mechanism. The present study did not consider the blood flow increase induced by vasodilatation resulting from the temperature rise,[76] which would have further reduced laser-induced heating of the skin as a result of the normal physiological thermoregulation processes. In addition, the superficial brain is spontaneously cooled by the environment and is cooler than arterial blood. Under physiological conditions, an increase in CBF may lead to an increase in superficial brain temperature and a simultaneous decrease in deep brain temperature, emphasizing the complexity of the effects of blood perfusion rate.

Our results show that changes in cerebral metabolism had no significant impact on local brain temperature changes congruent with the experimental results[77] [Fig. 5(b)]. However, changes in brain temperature were linked with cerebral blood perfusion and blood perfusion contributed to maintain a low brain temperature.

4.4 Effect of Various Skin and Brain Absorption and Scattering Coefficients

Discordant values have been reported for the exact absorption and scattering coefficients. These discordant values could be due to the discrepancies between theoretical and experimental investigations. In general, *in vivo* μ_a and μ_s values for human skin are significantly lower than those obtained *in vitro* (about 10-fold and twofold lower, respectively[71]). The discordant values for μ_a may be related to the low sensitivity of the double-integrating sphere, the goniometric techniques used for *in vitro* measurements at low absorption combined with strong scattering ($\mu_a \ll \mu_s$) and sample preparation methods.[71] Consequently, in the absence of accurate absorption coefficients, these values need to be chosen cautiously, and our temperature profiles were probably overestimated as data were presented as the maximum temperature rise resulting from intentional selection of the maximum absorption coefficients available in the literature. As skin absorption is usually dominated by melanin absorption, various melanin levels in the skin have, therefore, been investigated to study the effect of darker skin. Figure 6 presents the temperature distributions with broad ranges of skin [Fig. 6(a)] and brain [Fig. 6(b)] absorption coefficients and shows that changes in brain or skin absorption coefficients had a greater impact on superficial layers closer to the source, and a lesser impact on deeper tissues. Nevertheless, as the brain is situated far from the source, this impact is limited to the brain surface [Fig. 6(b), inset].

Photons are less scattered and penetrate much more deeply for lower values of scattering coefficient, as they are able to travel over a longer distance with a greater step size before they interact with the tissue at a new position. As the value of the scattering coefficient increases, scattering increases and photons undergo frequent scattering with smaller step sizes, resulting in a more circular profile of fluence rate. For lower

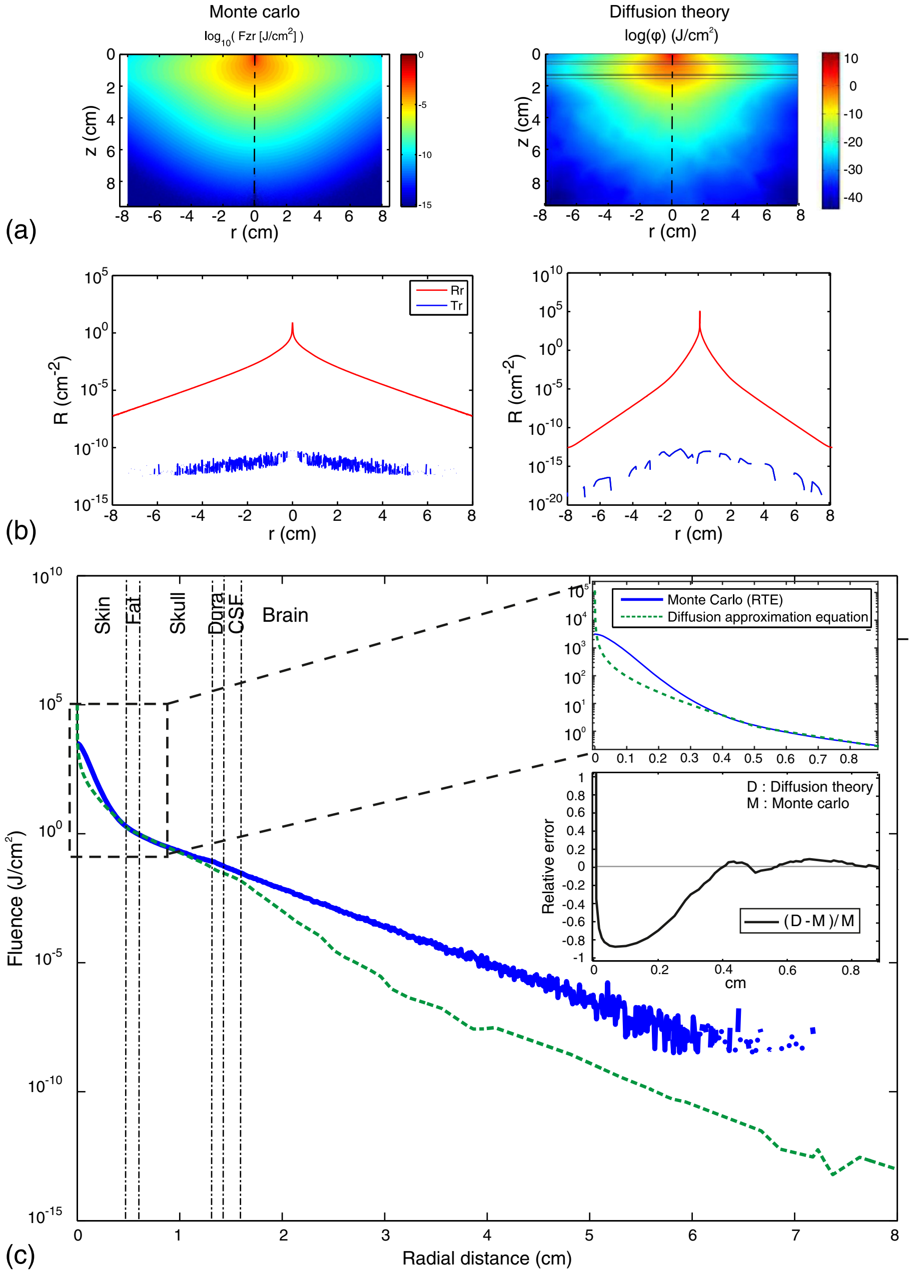

Fig. 10 Comparisons between the Monte Carlo method and the diffusion theory in terms of (a) distribution of fluence rate, (b) the diffuse reflectance, transmittance. (c) Fluence J/cm^2 (the inset shows relative errors between the results of the Monte Carlo method and the diffusion theory).

scattering coefficients, photons penetrate much more deeply with intensity decreasing outward according to the radial distance. While changes in scattering coefficients can impact the photon density distribution, their effect on temperature is negligible in view of the fact that the range of scattering coefficients of these head layers is low (brain scattering coefficient, 8.74 to 12.17 cm^{-1}; skin, 15.09 to 26.75 cm^{-1}; fat, 8.30 to 22.12 cm^{-1}; skull, 8.89 to 19.24 cm^{-1}; and CSF, 0.1 to 3.2 cm^{-1}).[67,70]

4.5 *Effect of Various Laser Spot Sizes*

The mechanisms involved in the interaction between laser and biological tissue are also intimately related to the laser characteristics (e.g., wavelength, energy density, and spot size). By increasing the beam spot size, laser light can be diffused over larger areas and, in these situations, laser power can be increased while maintaining safe levels of skin irradiation. Figure 7 shows that the temperature decreased as the laser spot size increased from 0.2 to 15 mm. This figure shows that, for a specific laser power, laser spot size should be kept above a specific limit to avoid skin temperatures exceeding safety limits (e.g., in adults, assuming a skin safety threshold of 10°C, if laser power = 100 mW, the spot size should be ≥11 mm).

In the brain, a few orders of magnitude of difference in spot size does not induce any change of brain temperature, but smaller differences in laser power cause measurable differences in brain temperature due to smaller spot size leading to higher irradiance but smaller penetration depth. Laser beam spot size determines the depth of penetration. A larger spot size decreases scattering of light and increases the depth of penetration. A larger spot size, therefore, results in deeper penetration, whereas a smaller spot size induces more rapid scatter and more rapid decay of fluence with depth.[78] Since the e^{-1} depth of scattered light is unclear when scattering dominates absorption ($\mu_a \ll \mu_s'$), the exact depth of light penetration in tissue has not been determined.[19] Therefore, by maintaining the same power, using a larger spot size (sp $\uparrow$) decreases irradiance ($I \downarrow$), but increases the depth of penetration of the light (depth $\uparrow$), resulting in insignificant temperature changes in deeper tissues (e.g., brain). By maintaining the same spot size, higher power ($P \uparrow$) increases irradiance ($I \uparrow$) and the depth of penetration of the light (depth $\uparrow$), resulting in significant brain temperature changes. The temperature in the brain thus depends on the laser power more than on the spot size.

Figures 7(a) and 7(b) show that spot size changes at constant power have a lesser intense heating effect on deeper tissue.

Figure 8 illustrates the temperature changes versus irradiance and shows higher temperature due to higher power and higher spot size with the same irradiance. In skin tissue, for small spot sizes, cooling of surrounding nonirradiated tissue is much more effective than for a large spot size. With larger spot sizes, heat transfer from the center of the spot size cannot occur radially (sideways). Consequently, for the same level of skin irradiance, larger spots produce higher temperatures than smaller spots. This effect of higher temperatures for larger spot sizes reduces the exposure limit, since the effect of cooling means that the damage threshold does not simply depend on the skin irradiance. Exposure limits decrease with increasing spot sizes, reflecting the fact that, for the same level of irradiance, larger spots are more hazardous than smaller spots. However, this dependence of the risk threshold on spot size diameter does not apply to very large spot sizes, since the temperature profile in the center of the spot has a more or less flat profile, and this value is not affected by any further increase in the actual spot size, as the edges that are cooled radially are situated too far away from the center. Consequently, for large sources, the risk threshold depends only on the irradiance and no longer on the spot diameter.[79]

For exposure to IR radiation of the skin lasting for several seconds, involuntary body movements and heat conduction disperse the irradiance profile over an area of at least several square millimeters (~3.5 mm), even when the irradiated body part is intentionally kept still, even the smaller spot sizes (0.2 to 1 mm) has been considered in our model in order to study the effect of these range of spot size (i.e., which is below the 10°C limit skin temperature at 3 mm but not below the 10°C limit at 1 mm at the same power). For the wavelength of 800 nm used in our study, with the maximum anticipated exposure time (Table 1) and an ANSI standard MPE equal to $0.3\ \mathrm{W/cm^{-2}}$, a larger power would be allowable with a larger spot size.

4.6 *Systematic Model Errors*

Our simulated model remains a mathematical model, meaning that errors could be come from the simplifications. These errors are essentially due to the following causes:

- The inaccuracy of the optical and thermal properties is the main point in the model's set of equations, as these properties are essential for the accuracy of the simulated model's outcome. Many approaches have been demonstrated to estimate these properties, but various authors have reported very discordant values reflecting the difficulty of estimating these properties. In addition, the inaccuracy is further increased by the dependency of the properties on the various parameters (temperature) over time, resulting in a nonlinear difference.
- The error of Pennes' bioheat equation is that it does not account for directionality of blood perfusion, which is an important factor in the energy exchange between vessels and tissue. In addition, Pennes' equation does not consider the local vascular geometry. While Pennes' bioheat model is based on incorrect anatomical views about the temperature distribution of blood through the tissues, it is still universally employed and its relative accuracy in tissue situated away from large vessels which introduce local convection has been confirmed.[80]
- Another error is related to computer performance limitations: accessible memory, the size of mesh nodes used to make the model. Our simulated model was established on the basis of the above conditions, with COMSOL standard refining processes at the crucial areas (around the heat source).
- Absolute numeric tolerance: Whole numerical approaches have a permitted error (absolute numeric tolerance) that expresses the reference point of the convergence. Different solvers commonly use different absolute tolerances. In our model, we used the COMSOL default tolerance value of 0.01 which leads to a final error of 1%, considered to be a reasonable criterion for modeling.
- Diffusion theory limit: Despite the fact that diffusion theory suggests a fast approach, it is not valid close to the light source or at the boundary where the photon intensity is strongly anisotropic. This is due to the fact that, at short distances, the radiance rate is not linearly anisotropic and the basic assumptions required for the diffusion approximation to the Boltzman transport equation are not satisfied. On the other hand, strong absorption prevents photons from engaging in an extended random walk and the approximation $\mu_t = \mu_s'$ becomes insufficient. The diffusion approximation is, therefore, only valid in highly scattering media (i.e., $\mu_a \ll \mu_s'$) and when the point of interest is situated far from sources or boundaries.
- The simulated head model consists of six types of tissues. However, the sophisticated geometry of the tissue structure is ignored and tissue layers are parallel to each other. In a real head, the thickness of superficial tissue, such as the scalp and skull, is not uniform and the brain surface is folded with sulci. The thickness of the skull is known to vary significantly around the head and between individuals. In addition, the thickness of the CSF can vary because the brain can move to a limited degree within the skull; this change is more prominent in the neonatal head. Moreover, there is a relationship between skin thickness and the neonate's gestational maturity.[50]

5 Conclusion

A laser–tissue interaction model was developed to predict the spatial dynamic changes in temperature rise during laser exposure of human head tissues. We describe the bases necessary to calculate the effects of the temperature changes caused by the absorption of light energy in the tissues, using the bioheat equation and including the cooling effects of blood perfusion in tissue in order to model the photothermal interaction of NIR laser on human tissues.

The temperature changes of the radiated zone calculated from our simulation and *in vitro* experiments presented a small deviation. Two of the main reasons for this deviation are the lack of accurate values of the tissue optical properties and diffusion approximation theory in superficial surfaces.

Further studies under different conditions are necessary to achieve full agreement with *in vivo* data, and, if necessary, define error correction factors to be added to the equation set. However, this would not eliminate the need for precise values for the optical and thermal properties of the tissue. On the other hand, our model remains practical, as it introduces a step in using simulated head tissues as a basis for much more detailed NIR laser photothermal interaction experiments.

The results presented in this work should be useful to optimize laser spot size and power for a variety of laser applications of functional imaging systems (e.g., DCS which need NIR light with relatively high laser power). A combination of simulation and adequate *in vitro* experiments could help to develop a more effective optical imaging to avoid any possible tissue damage.

References

1. F. Scholkmann et al., "A review on continuous wave functional near-infrared spectroscopy and imaging instrumentation and methodology," *NeuroImage* **85**(1), 6–27 (2014).
2. K. Izzetoglu et al., "Functional near-infrared neuroimaging," in *Annual Int. Conf. of the IEEE Engineering in Medicine and Biology Society*, Vol. 7, pp. 5333–5336 (2004).
3. L. Goldman, "Dye laser principles: with applications," in *Dye Laser Principles*, F. J. Duarte and L. W. Hillman, Eds., Academic Press, New York (1990).
4. F. J. Duarte, *Tunable Laser Applications*, 2nd ed., pp. 245–280, CRC Press, New York (2008).
5. M. Ferrari and V. Quaresima, "A brief review on the history of human functional near-infrared spectroscopy (fNIRS) development and fields of application," *NeuroImage* **63**(2), 921–935 (2012).
6. H. Obrig, "NIRS in clinical neurology—a 'promising' tool?" *NeuroImage* **85**(1), 535–546 (2014).
7. N. Roche-Labarbe et al., "Coupled oxygenation oscillation measured by NIRS and intermittent cerebral activation on EEG in premature infants," *NeuroImage* **36**(3), 718–727 (2007).
8. M. Mahmoudzadeh et al., "Syllabic discrimination in premature human infants prior to complete formation of cortical layers," *Proc. Natl. Acad. Sci. U. S. A.* **110**(12), 4846–4851 (2013).
9. T. Durduran et al., "Diffuse optics for tissue monitoring and tomography," *Rep. Prog. Phys.* **73**(7), 076701 (2010).
10. F. J. Duarte et al., *Dye Laser Principles: With Applications*, Elsevier Science, Boston (2012).
11. M. Manoochehri et al., "Light on: neural shrinking and swelling, in vivo, around epileptic changes," submitted.
12. N. Roche-Labarbe et al., "Noninvasive optical measures of CBV, StO_2, CBF index, and $rCMRO_2$ in human premature neonates' brains in the first six weeks of life," *Hum. Brain Mapp.* **31**(3), 341–352 (2010).
13. D. A. Boas, L. E. Campbell, and A. G. Yodh, "Scattering and imaging with diffusing temporal field correlations," *Phys. Rev. Lett.* **75**(9), 1855–1858 (1995).
14. D. A. Boas and A. G. Yodh, "Spatially varying dynamical properties of turbid media probed with diffusing temporal light correlation," *J. Opt. Soc. Am. A* **14**(1), 192–215 (1997).
15. D. J. Pine et al., "Diffusing wave spectroscopy," *Phys. Rev. Lett.* **60**(12), 1134–1137 (1988).
16. P. Y. Lin et al., "Non-invasive optical measurement of cerebral metabolism and hemodynamics in infants," *J. Visualized Exp.* **73**, e4379 (2013).
17. D. F. Milej et al., "Assessment of ICG inflow to the brain by time-resolved measurements of diffuse reflectance at 16 source–detector separations," in *Biomedical Optics 2014*, paper BM3A.23, Optical Society of America, Miami, Florida (2014).
18. R. Dua and S. Chakraborty, "A novel modeling and simulation technique of photo-thermal interactions between lasers and living biological tissues undergoing multiple changes in phase," *Comput. Boil. Med.* **35**(5), 447–462 (2005).
19. A. J. Welch and M. J. C. van Gemert, *Optical-Response of Laser-Irradiated Tissue*, Springer, Plenum, New York (1995).
20. M. Ganguly, *Analyzing Thermal and Mechanical Effects of Pulsed Laser Irradiation on Tissues*, Biomedical Department, Florida Institute of Technology, Melbourne, Florida (2012).
21. T. Fujii and Y. Ibata, "Effects of heating on electrical activities of guinea pig olfactory cortical slices," *Pflugers Arch.* **392**(3), 257–260 (1982).
22. T. M. Seese et al., "Characterization of tissue morphology, angiogenesis, and temperature in the adaptive response of muscle tissue to chronic heating," *Lab. Invest.* **78**(12), 1553–1562 (1998).
23. A. C. Thompson et al., "Modeling of light absorption in tissue during infrared neural stimulation," *J. Biomed. Opt.* **17**(7), 075002 (2012).
24. J. C. LaManna et al., "Stimulus-activated changes in brain tissue temperature in the anesthetized rat," *Metab. Brain Dis.* **4**(4), 225–237 (1989).
25. W. C. Dewey et al., "Cellular responses to combinations of hyperthermia and radiation," *Radiology* **123**(2), 463–474 (1977).
26. Y. Ito et al., "Assessment of heating effects in skin during continuous wave near infrared spectroscopy," *J. Biomed. Opt.* **5**(4), 383–390 (2000).
27. J. H. Kim, E. W. Hahn, and P. P. Antich, "Radiofrequency hyperthermia for clinical cancer therapy," *Nat. Cancer Inst. Monogr.* **61**, 339–342 (1982).
28. S. W. Jeong, H. Liu, and W. R. Chen, "Temperature control in deep tumor treatment," *Proc. SPIE* **5068**, 210–216 (2003).
29. A. J. Vander, J. H. Sherman, and D. S. Luciano, *Human Physiology: The Mechanisms of Body Function*, McGraw-Hill, New York (2001).
30. M. Ueda, J. Bures, and J. Fischer, "Spreading depression elicited by thermal effects of ultrasonic irradiation of cerebral cortex in rats," *J. Neurobiol.* **8**(4), 381–393 (1977).
31. M. Denda, M. Tsutsumi, and S. Denda, "Topical application of TRPM8 agonists accelerates skin permeability barrier recovery and reduces epidermal proliferation induced by barrier insult: role of cold-sensitive TRP receptors in epidermal permeability barrier homoeostasis," *Exp. Dermatol.* **19**(9), 791–795 (2010).
32. M. Cope and D. T. Delpy, "System for long-term measurement of cerebral blood and tissue oxygenation on newborn infants by near infra-red transillumination," *Med. Biol. Eng. Comput.* **26**(3), 289–294 (1988).
33. A. Bozkurt and B. Onaral, "Safety assessment of near infrared light emitting diodes for diffuse optical measurements," *Biomed. Eng. Online* **3**(1), 9 (2004).
34. A. N. S. Institute, *American National Standard for Safe Use of Lasers ANSI Z136.1*, Laser Institute of America, Orlando, Florida (2014).
35. K. Schröder, *Handbook on Industrial Laser Safety*, Technical University of Vienna, Vienna (2000).
36. "Laser standards and classifications," 2015, https://www.rli.com/resources/articles/classification.aspx.
37. International Commission On Non-Ionizing Radiation Protection (ICONIR), "ICNIRP guidelines on limits of exposure to laser radiation of wavelengths between 180 nm and 1,000 μm," *Health Phys.* **105**(3), 271–295 (2011).
38. H. H. Pennes, "Analysis of tissue and arterial blood temperatures in the resting human forearm," *J. Appl. Physiol.* **1**(2), 93–122 (1948).
39. S. Kim et al., "Thermal impact of an active 3-D microelectrode array implanted in the brain," *IEEE Trans. Neural Syst. Rehabil. Eng.* **15**(4), 493–501 (2007).
40. "Comsol AB: COMSOL multiphysics 3.2b user's guide," FEMLAB Tutorial (2006).
41. A. Saouli and K. Mansour, "Modelling of the near infra-red radiation pulse propagation in biological tissues for medical imaging application," *J. Intense Pulsed Lasers Appl. Adv. Phys.* **3**(4), 41–45 (2013).

42. T. J. Farrell and M. S. Patterson, "Experimental verification of the effect of refractive index mismatch on the light fluence in a turbid medium," *J. Biomed. Opt.* **6**(4), 468–473 (2001).
43. L. Gobin, L. Blanchot, and H. Saint-Jalmes, "Integrating the digitized backscattered image to measure absorption and reduced-scattering coefficients in vivo," *Appl. Opt.* **38**(19), 4217–4227 (1999).
44. M. Kiguchi et al., "Comparison of light intensity on the brain surface due to laser exposure during optical topography and solar irradiation," *J. Biomed. Opt.* **12**(6), 062108 (2007).
45. A. H. Bamett et al., "Robust inference of baseline optical properties of the human head with three-dimensional segmentation from magnetic resonance imaging," *Appl. Opt.* **42**(16), 3095–3108 (2003).
46. S. J. Madsen, *Optical Methods and Instrumentation in Brain Imaging and Therapy*, Springer, New York (2012).
47. Y. Rahmat-Samii and K. W. Kim, "Antennas and human in personal communications: applications of modern EM computational techniques," in *12th Int. Conf. on Microwaves and Radar (MIKON '98)*, Vol. 34, pp. 36–55 (1998).
48. H. Khodabakhshi and A. Cheldavi, "Irradiation of a six-layered spherical model of human head in the near field of a half-wave dipole antenna," *IEEE Trans. Microwave Theory Tech.* **58**(3), 680–690 (2010).
49. É. A. Genina et al., "Optical clearing of human dura mater," *Opt. Spectrosc.* **98**(3), 470–476 (2005).
50. I. S. Saidi, *Transcutaneous Optical Measurement of Hyperbilirubinemia in Neonates*, Rice University, Houston (1992).
51. X. Ronghou et al., "Study on generalized thermoelastic problem of semi-infinite plate heated locally by the pulse laser," *IJEPR* **3**(4) (2014).
52. S. C. DeMarco et al., "Computed SAR and thermal elevation in a 0.25-mm 2-D model of the human eye and head in response to an implanted retinal stimulator—part I: models and methods," *IEEE Trans. Antennas Propag.* **51**(9), 2274–2285 (2003).
53. Tissue Properties, 2015, www.itis.ethz.ch/itis-for-health/tissue-properties/database/database-summary/.
54. P. Bernardi et al., "Specific absorption rate and temperature increases in the head of a cellular-phone user," *IEEE Trans. Microwave Theory Tech.* **48**(7), 1118–1126 (2000).
55. L. R. Williams and R. W. Leggett, "Reference values for resting blood flow to organs of man," *Clin. Phys. Physiol. Meas.* **10**(3), 187–217 (1989).
56. F. A. Duck, *Physical Properties of Tissues: A Comprehensive Reference Book*, Academic Press, London (1990).
57. D. I. Altman et al., "Cerebral blood flow requirement for brain viability in newborn infants is lower than in adults," *Ann. Neurol.* **24**(2), 218–226 (1988).
58. A. D. Edwards et al., "Cotside measurement of cerebral blood flow in ill newborn infants by near infrared spectroscopy," *Lancet* **332**(8614), 770–771 (1988).
59. T. Kusaka et al., "Cerebral distribution of cardiac output in newborn infants," *Arch. Dis. Childhood Fetal Neonatal Ed.* **90**(1), F77–F78 (2005).
60. M. Rowland and T. N. Tozer, *Clinical Pharmacokinetics: Concepts and Applications*, Williams & Wilkins, Baltimore (1995).
61. L. Shargel, S. Wu-Pong, and A. Yu, *Applied Biopharmaceutics & Pharmacokinetics*, 5th ed., McGraw-Hill Education, The University of Michigan (2004).
62. S. Iwata et al., "Dual role of cerebral blood flow in regional brain temperature control in the healthy newborn infant," *Int. J. Dev. Neurosci.* **37**, 1–7 (2014).
63. R. A. Kauppinen et al., "Assessment of human brain temperature by ^{1}H MRS during visual stimulation and hypercapnia," *NMR Biomed.* **21**(4), 388–395 (2008).
64. R. G. Gordon, R. B. Roemer, and S. M. Horvath, "A mathematical model of the human temperature regulatory system-transient cold exposure response," *IEEE Trans. Biomed. Eng.* **23**(6), 434–444 (1976).
65. P. Scheinberg et al., "Effects of vigorous physical exercise on cerebral circulation and metabolism," *Am. J. Med.* **16**(4), 549–554 (1954).
66. T. Vo-Dinh, *Biomedical Photonics Handbook*, 2nd ed., Taylor & Francis, CRC Press, Boca Raton, Florida (2014).
67. S. L. Jacques, "Optical properties of biological tissues: a review," *Phys. Med. Biol.* **58**(11), R37–R61 (2013).
68. I. S. Saidi, *Transcutaneous Optical Measurement of Hyperbilirubinemia in Neonates*, Rice University (1992).
69. P. van der Zee, M. Essenpreis, and D. T. Delpy, "Optical properties of brain tissue," *Proc. SPIE* **1888** 454–465 (1993).
70. E. Okada and D. T. Delpy, "Near-infrared light propagation in an adult head model. I. Modeling of low-level scattering in the cerebrospinal fluid layer," *Appl. Opt.* **42**(16), 2906–2914 (2003).
71. V. Tuchin and So. P.-o. I. Engineers, *Tissue Optics: Light Scattering Methods and Instruments for Medical Diagnosis*, SPIE Press, Bellingham, Washington (2007).
72. Monte Carlo Simulations, 2007 http://omlc.org/software/mc/.
73. M. Motamedi et al., "Light and temperature distribution in laser irradiated tissue: the influence of anisotropic scattering and refractive index," *Appl. Opt.* **28**(12), 2230–2237 (1989).
74. E. P. Widmaier, H. Raff, and K. T. Strang, *Vander, Sherman, & Luciano's Human Physiology: The Mechanisms of Body Function*, McGraw-Hill Higher Education, The University of Michigan (2004).
75. D. R. Kenshalo and H. A. Scott Jr., "Temporal course of thermal adaptation," *Science* **151**(3714), 1095–1096 (1966).
76. N. Charkoudian, "Mechanisms and modifiers of reflex induced cutaneous vasodilation and vasoconstriction in humans," *J. Appl. Physiol.* **109**(4), 1221–1228 (2010).
77. G. Shafirstein et al., "Laser tissue interaction modeling for treatment planning of port-wine stain," in *The 16th Annual Meeting of the IEEE Lasers and Electro-Optics Society (LEOS)*, Vol. 311, pp. 313–315 (2003).
78. M. Keijzer et al., "Light distributions in artery tissue: Monte Carlo simulations for finite-diameter laser beams," *Lasers Surg. Med.* **9**(2), 148–154 (1989).
79. R. Henderson and K. Schulmeister, *Laser Safety*, Taylor & Francis, Institute of Physics, Bristol (2004).
80. H. Arkin, L. X. Xu, and K. R. Holmes, "Recent developments in modeling heat transfer in blood perfused tissues," *IEEE Trans. Biomed. Eng.* **41**(2), 97–107 (1994).

Biographies for the authors are not available.